

Comparison of multi-compartment cable models of human auditory nerve fibers

Richard Bachmaier¹, Jörg Encke^{1,2,3}, Miguel Obando-Leitón^{1,2,4}, Werner Hemmert^{1,2,4} and Siwei Bai^{1,2,5,*}

¹Department of Electrical and Computer Engineering, Technical University of Munich, 80333 Munich, Germany

²Munich School of Bioengineering, Technical University of Munich, 85748 Garching, Germany

³Medizinische Physik and Cluster of Excellence Hearing4all, Universität Oldenburg, 26111, Oldenburg, Germany

⁴Graduate School of Systemic Neurosciences, Ludwig Maximilian University of Munich, 82152 Planegg, Germany

⁵Graduate School of Biomedical Engineering, University of New South Wales, Sydney, NSW 2052, Australia

Correspondence*:
Siwei Bai
siwei.bai(at)tum.de

2 ABSTRACT

3 Background: Multi-compartment cable models of auditory nerve fibers have been developed to
4 assist the improvement of cochlear implants. With the advancement of computational technology
5 and the results obtained from in vivo and in vitro experiments, these models have evolved to
6 incorporate a considerable degree of morphological and physiological details. They have also
7 been combined with three-dimensional volume conduction models of the cochlea to simulate
8 neural responses to electrical stimulation. However, no specific rules have been provided on
9 choosing the appropriate cable model, and most models adopted in recent studies were chosen
10 without a specific reason or by inheritance.

11 Methods: Three of the most cited biophysical multi-compartment cable models of the human
12 auditory nerve, i.e. Rattay et al., Briaire and Frijns, and Smit et al., were implemented in this
13 study. Several properties of single fibers were compared among the three models, including
14 threshold, conduction velocity, action potential shape, latency, refractory properties, as well as
15 stochastic and temporal behaviors. Experimental results regarding these properties were also
16 included as a reference for comparison.

17 Results: For monophasic single-pulse stimulation, the ratio of anodic versus cathodic thresholds
18 in all models was within the experimental range, despite a much larger ratio in the model by
19 Briaire and Frijns. For biphasic pulse-train stimulation, thresholds as a function of both pulse rate
20 and pulse duration differed between the models, but none matched the experimental observations
21 even coarsely. Similarly, for all other properties including the conduction velocity, action potential
22 shape, and latency, the models presented different outcomes and not all of them fell within the
23 range observed in experiments.

24 Conclusions: While all three models presented similar values in certain single fiber properties
25 to those obtained in experiments, none matched the experimental observations satisfactorily.
26 In particular, the adaptation and temporal integration behaviors were completely missing in all
27 models. Further extensions and analyses are required to explain and simulate realistic auditory
28 nerve fiber responses to electrical stimulation.

29 **Keywords:** Auditory nerve, computational model, biophysical, cable model, electrical stimulation, threshold

1 INTRODUCTION

30 Multi-compartment cable models of the auditory nerve fibers (ANF) have been developed to assist in
31 understanding and predicting neural responses to external stimulation. They have been used to advance
32 our knowledge regarding how the auditory nerve encodes timing, frequency and intensity information
33 (Imennov and Rubinstein, 2009). Moreover, multi-compartment ANF models have been combined with
34 three-dimensional volume conduction models of the cochlea to simulate responses to cochlear implant
35 (CI) stimulation (Kalkman et al., 2015; Malherbe et al., 2016; Nogueira and Ashida, 2018). Alongside
36 psychophysical experiments, computational models of the auditory nerve are used to evaluate new sound
37 coding and stimulation strategies and are therefore crucial for the improvement of CIs. Nevertheless,
38 there exist several ANF models in the literature with varying morphological or ionic channel properties.
39 Choosing the appropriate cable model for a given computational study is difficult as the different models
40 are difficult to compare based on the original publications. Consequently, most models adopted in existing
41 studies were chosen without a specific reason or by inheritance.

42 Generally speaking, multi-compartment models are morphological extensions of single-node models.
43 Based on the Schwarz–Eikhof (SE) node model of rat and feline ion channel kinetics (Schwarz and Eikhof,
44 1987), Frijns et al. (1994) developed an axon model, which was subsequently extended with dendrite and
45 soma to match the feline ANF morphology (Frijns et al., 1995). However, differences in morphology
46 between human and cat might impact spike travel time, and this must be taken into account for correct
47 predictions of CI stimulus coding in humans (Rattay et al., 2001; O’Brien and Rubinstein, 2016). Therefore,
48 this feline ANF model was later modified to account for the human ANF morphology (Briaire and Frijns,
49 2005). Meanwhile, Rattay et al. (2001) designed a different human ANF model based on Hodgkins and
50 Huxleys (HH) description of the unmyelinated squid axon (Hodgkin and Huxley, 1952) while also including
51 human ANF morphology. Smit et al. (2008) adopted the dendrite and soma from Rattay et al. (2001), but
52 modified the properties of the axon in order to account for differences in membrane currents at the node of
53 Ranvier between human (Schwarz et al., 1995) and squid.

54 In addition to differences in morphology and ion channel properties, some ANF cable models also
55 include modifications in order to implement specific physiological properties, including stochastic effects
56 and adaptation. For instance, Rattay et al. (2001) incorporated a simple and efficient approach to predict
57 stochastic ANF responses by adding a Gaussian noise current term to the total ion current. In comparison,
58 Imennov and Rubinstein (2009) and Negm and Bruce (2014) represented the stochastic nature of ion
59 channels by applying a channel-number tracking algorithm. Woo et al. (2010) included a model of rate
60 adaptation based on a dynamic external potassium concentration, whereas van Gendt et al. (2016) integrated
61 their biophysical model with a phenomenological approach to simulate threshold fluctuations, adaptation
62 and accommodation.

63 Differences in the description of ANF morphology and physiology lead to distinct model characteristics.
64 A meaningful comparison based on the respective publications is however not feasible, as the models

were only fitted to specific ANF properties under certain stimulation patterns. For example, Rattay et al. (2001) detailed the initiation and propagation of action potentials (APs), but did not describe properties like the strength-duration relation and refractory period. Frijns et al. (1994) and Smit et al. (2008) measured the AP shape, conduction velocity, strength-duration relation and refractory period, but none of these properties was mentioned for the updated versions of their model in Briaire and Frijns (2005) and Smit et al. (2010). Studies that included an adaptation mechanism in their ANF cable models, investigated almost exclusively responses to pulse-train stimulation, but did not include single-pulse responses as in other studies. Therefore, it is necessary to compare the spiking characteristics of different ANF models in order to investigate how the models behave with more generalised stimuli. In this study, the three often cited biophysical human ANF cable models. The Rattay (RA) model from Rattay et al. (2001), the Briaire-Frijns (BF) model from Briaire and Frijns (2005) and the Smit-Hanekom (SH) model from Smit et al. (2010), were chosen and implemented in a consistent framework, and their performance was evaluated by comparing them against experimental data.

2 METHODS

The multi-compartment ANF models by Rattay et al. (2001), Briaire and Frijns (2005) and Smit et al. (2010), from here on abbreviated as RA, BF and SH, respectively, were implemented in a single framework using Python 3.4, with the package Brian2 (Goodman and Brette, 2009). All models followed the morphology of a human ANF as described in the original publication and consisted of dendrite, soma, and axon. Dendrite and axon were composed of an alternating structure of active nodes and passive myelinated internodes. Additionally, all models included a peripheral terminal as well as a pre-somatic region. All morphological components were modelled as electrical circuits and represented by cylindrical compartments. The spherical shape of the somas in the RA and SH models was approximated by segmenting it into ten cylindrical compartments. Compartment lengths and diameters were distinct in each model, as shown in Fig 1. Details of the morphologies can be taken from their respective publications. The length of dendritic internodes in Briaire and Frijns (2005) was defined as scalable so as to reflect the varied lengths from the organ of Corti to the soma. In this study, the dendritic internodes were scaled as suggested by Kalkman et al. (2014) with a maximum length of 250 μm .

In unmyelinated compartments of the ANF models, the cell membrane was represented by a capacitor which was charged or discharged by ionic currents. These currents depended on membrane's ionic permeabilities and Nernst potentials of individual ion species. All three models included exclusively sodium and potassium channels. The BF model utilised the gating properties suggested by Schwarz and Eikhof (1987) and calculated the ionic currents according to Frankenhaeuser and Huxley (1964), whereas RA and SH adopted the gating properties and equations proposed by Hodgkin and Huxley (1952). However, compared to the original gating properties of the Hodgkin-Huxley (HH) kinetics, which were measured in a squid at 6.3 $^{\circ}\text{C}$, in the RA and SH models they were each multiplied by a compensating factor to account for the faster gating processes in mammalian nerve fibers, and the ionic channel densities were increased. Furthermore, in order to specifically account for the human ANF physiology, Smit et al. (2010) added two modifications to the HH ion channels in the axon: *a*) the opening and closing of the potassium channels were modified to be slower (Smit et al., 2008); *b*) a persistent sodium current was added to account for the total sodium current together with a transient one of the original HH model (Smit et al., 2009). While the models by Briaire and Frijns (2005) and Smit et al. (2010) are deterministic, Rattay et al. (2001) incorporated a simple approach to predict stochastic ANF responses by adding a Gaussian noise

current term to the total ion current. It was calculated with:

$$i_{noise} = X \cdot k_{noise} \sqrt{A g_{Na}}, \quad (1)$$

where X is a Gaussian random variable (mean=0, S.D.=1). g_{Na} denotes the maximum sodium conductivity, and A is the membrane surface area. The term is multiplied with the factor k_{noise} , which is common to all compartments and is used to adjust how strongly the stochastic behavior of the channels is emphasized. In this study, we decided to add the noise term to all three models to investigate the feasibility of this approach to simulate stochasticity and to compare the models also with stochasticity.

Regarding the passive internodes, Briaire and Frijns (2005) implied that they were surrounded by a perfectly insulating myelin sheath. As a consequence, both their capacity and conductivity were assumed to be zero; whereas Rattay et al. (2001) described them as a passive resistor-capacitor network and thus as imperfect insulators. In Smit et al. (2010), the dendritic internodes were modeled following Rattay et al. (2001), but the axonal internodes were described using a double-cable structure as proposed by Blight (1985). Detailed information regarding the ionic models can again be found in the respective publications.

The extracellular space of the ANF models was simulated as a homogeneous medium with an isotropic resistivity of $3 \Omega \text{ m}$. Unless otherwise stated, each fiber was stimulated externally by a point electrode situated above the third dendritic node with a vertical distance of $500 \mu\text{m}$ to the fiber. Measurements were performed at the tenth axonal node to ensure the propagation of an action potential (AP) to the axon. Several properties of single ANF were compared among the three models, including threshold, conduction velocity, AP shape, latency, refractory properties, as well as stochastic and temporal behaviors.

For each of the properties investigated here, the parameters for the applied stimuli were taken from the respective physiological experiments in order to ensure a meaningful comparison with experimental results in the literature. Whenever a biphasic stimulus was administered, it was always cathodic-first.

3 RESULTS

3.1 Thresholds

The threshold current I_{th} of an ANF model is defined as the minimal current amplitude required to elicit an AP with otherwise constant stimulation parameters. This section reports the dependency of I_{th} on the phase length and polarity of single monophasic pulses, the pulse rate and duration of biphasic pulse trains, and the frequency and duration of sinusoidal stimuli.

3.1.1 Single monophasic pulses

Figure 2 compares the strength-duration curves, i.e. the relations between I_{th} and the duration of the applied pulse, for both monophasic cathodic and anodic stimuli. All models demonstrated thresholds that decrease with longer pulse duration. Thresholds were also larger for anodic stimulation; this was most obvious for the BF model.

The current threshold to which a strength-duration curve converges for a very long pulse is called rheobase I_{rh} ; the chronaxie τ_{chr} defines the required pulse width to elicit an AP when applying twice I_{rh} . These two values are commonly used to characterize the strength-duration behavior of a nerve fiber and are compared among the three models in Table 1. The values for I_{rh} with cathodic stimuli ranged from $61.3 \mu\text{A}$ (RA) to $220 \mu\text{A}$ (BF), and were smaller than those with anodic pulses. While I_{rh} for the two polarities differed by a factor of 1.4 and 1.2 for the RA and SH model, the threshold for anodic stimulation increased by more than

a factor of 2.1 in the BF model. The impact of polarity on τ_{chr} was less pronounced, and the values ranged from 39.1 μs (BF) to 125 μs (RA).

In Ranck (1975), τ_{chr} of mammalian nerve fibers were found to lie between 29 μs and 100 μs , whereas Van den Honert and Stypulkowski (1984) suggested a distinctly longer average chronaxie of 264 μs based on experiments with feline ANF. Variations in these experimental observations may be due to differences in experimental setup and stimulation method (Frijns et al., 1994). BeMent and Ranck (1969) measured that anodic pulses required 3.19–7.7 times the current of cathodic pulses to excite feline nerve fibers, and Armstrong et al. (1973) reported a ratio of 1.0–3.2. Therefore, despite the large variation between the three models, all of them show τ_{chr} within the experimental range and all three are consistent with the increased anodic thresholds.

3.1.2 Biphasic pulse trains

Trains of biphasic pulses with 45 μs /phase and an 8 μs inter-phase gap were applied to all ANF models. I_{th} was measured as a function of pulse rate and train duration, as depicted in Fig. 3. In all cases, the thresholds remained constant for pulse rates up to 2000 pulses per second (pps) and train durations longer than 1 ms. The RA model predicted a decreasing threshold for pulse rates higher than 2000 pps with a maximal drop of 1 dB from the single biphasic pulse threshold at 10 000 pps. SH, however, showed an opposite trend: the threshold at 10 000 pps rose by over 1 dB for all train durations longer than 0.3 ms. No obvious differences from the single pulse threshold were observed in BF.

Experiments with human CI listeners have also shown that thresholds decrease with pulse rates (multi-pulse integration). Carlyon et al. (2015) measured a drop of 3.9 dB from 71 pps to 500 pps and a larger drop of 7.7 dB from 500 pps to 3500 pps. Integration for pulse rates even smaller than 10 pps has been observed by (Zhou et al., 2015) who delivered pulse-train stimuli through CIs in humans and guinea pigs. They also discovered temporal integration up to 640 ms. Our simulation results thus lead to the conclusion that none of the models was able to predict pulse-train integration in a comparable range with the experimental data.

3.1.3 Sinusoidal stimulation

I_{th} was also measured for sinusoidal stimuli (positive phase first) with frequencies between 125 Hz and 16 kHz, as depicted in Fig. 4. All models predicted the minimal threshold at a frequency of 500 Hz. In RA, a growth of approximately 6 dB per octave was obtained for frequencies higher than 1 kHz, and a similar increase, namely 7 dB per octave, was found in SH above 2 kHz; in comparison, BF predicted smaller threshold increases between 1 and 8 kHz, between 8 and 16 kHz the slope was close to 7 dB per octave. Stimulus duration exerted only minimal impact on the threshold.

Dynes and Delgutte (1992) recorded threshold currents in cat auditory nerve fibers. While for high frequencies (8 kHz – 20 kHz), the slope of the threshold increase approaches 6 dB per octave in most fibers as in the models, for low frequencies (200 Hz – 1 kHz) the slope flattened only to about 3 dB per octave and never increased. Shannon (1983) measured the threshold of sinusoidal stimuli with frequencies between 30 Hz and 3 kHz in human CI users. The resulting threshold-frequency curve could be divided into three parts: a rather flat segment for frequencies below 100 Hz, a segment with an increase of 12–15 dB per octave at frequencies between 100 Hz and 300 Hz, and a 3 dB per octave increase segment for higher frequencies. Pfingst (1988) also reported an increase in the threshold of roughly 3 dB per octave for frequencies between 1 kHz and 16 kHz. Pfingst (1988) and Pfingst and Morris (1993) obtained threshold-frequency curves which dropped for small frequencies with a minimum threshold between 60 Hz and

184 200 Hz. Due to these differences, it must be concluded that the comparison of psychophysical threshold
185 and single fiber recordings/simulations must be taken with a grain of salt.

186 None of the ANF models predicted a threshold increase of more than 10 dB per octave as measured
187 by Shannon (1983) between 100 Hz and 300 Hz. The threshold-frequency curves predicted with the
188 models dropped between 125 Hz and 500 Hz so the minimum was reached for a higher frequency than in
189 experiments. The threshold increase measured from BF between 2 kHz and 8 kHz matched the experimental
190 results, whereas the other two models overestimated it by a factor of two.

191 In the absence of electrophysiological measurements however, psychoacoustic measurements might give
192 an insight into general trends.

193 3.2 Conduction velocity

194 The conduction velocity v_c describes how fast an AP propagates along the nerve fiber. Hursh (1939)
195 found in feline nerve fibers, that v_c increased linearly with the fiber outer diameter D , and reported the
196 scaling factor k to be 6. k is was defined as:

$$k = \frac{v_c / (\text{ms}^{-1})}{D / \mu\text{m}}. \quad (2)$$

197 Boyd and Kalu (1979) obtained a slightly smaller scaling factor of 4.6 for feline nerve fibers with an
198 outer diameter between 3 μm and 12 μm . Figure 5 compares the conduction velocities of ANF models
199 with experimental results. The velocities of dendrite and axon were measured separately due to their
200 morphological and physiological differences. Scaling factors for the dendrite of BF and the axon of SH
201 were considerably smaller than experimentally obtained values, while all other scaling factors were within
202 $\pm 25\%$ of the experimental results.

203 The soma of all three ANF models has a high capacitance due to its large diameter and reduced
204 myelination. Consequently, the soma delays the conduction of APs. This is apparent in Fig. 6, which
205 illustrates the model responses to a 100 μs cathodic current pulse injected at the peripheral terminal. The
206 duration of the somatic delay was determined by measuring the time difference between the APs at the
207 nodes directly before and after the soma, which were found to be 305 μs , 130 μs and 240 μs for RA, BF and
208 SH, respectively. Stypulkowski and Van den Honert (1984) measured the electrically evoked compound
209 AP of feline auditory nerves and observed two peaks with a time difference of 200 μs . They suggested that
210 the earlier peak arose from a direct excitation of the axon near the soma, whereas the second peak had its
211 origin at the dendrite. Accordingly, the time difference between the two peaks can be used to estimate the
212 somatic delay for feline ANFs, which is closer to the values from BF and SH. On the other hand, the double
213 peaks exhibited in neuronal response telemetry measurements with CI listeners have a temporal distance of
214 300 μs (Lai and Dillier, 2000). Using this value as a reference point for human ANFs, the somatic delay
215 predicted by RA appears very realistic.

216 3.3 Action potential shape

217 The shape of AP was compared among ANF models by measuring the height, as well as the rise and fall
218 times of AP. The AP height was defined as the voltage difference between the resting potential and the
219 peak value. Rise and fall times were determined as the time periods between the AP maximum and its 10 %
220 height, obtained during the ramp-up and -down phases, respectively. In this section, APs were triggered by
221 a monophasic 100 μs cathodic current pulse with an amplitude of I_{th} and $2 \times I_{\text{th}}$, as shown in Fig. 7.

The increase of the stimulus amplitude by a factor of two resulted in no significant changes in the AP shape in any of the models, but drastically shortened their latency, which is reported in Sec. 3.4. The short hyperpolarization at the beginning of the curves from BF was a passive response to the external cathodic stimulus, which is not visible in the other models. Another striking feature observed from Fig. 7 is the extremely long fall time of 712 μs with SH, which is more than three times as large as those with the other models. In comparison, the differences in AP height and rise time were relatively small: the AP height ranged from about 88 mV (RA) to 107 mV (SH), and all APs peaked at positive values; the rise time ranged from 87 μs (BF) and 121 μs (SH). These parameters that define the AP shape were almost independent of pulse form, phase duration and stimulus amplitude.

Only a limited number of studies with the objective to investigate AP shape can be found in the literature. Paintal (1966) measured AP rise and fall times of feline nerve fibers at 37.1 °C and revealed an inverse relation with the conduction velocity. The rise time curve was steep for a conduction velocity below 40 ms^{-1} and flattened out for faster conduction. On the other hand, the relation between the fall time and conduction velocity was approximately linear. Based on the conduction velocities reported in Sec. 3.2, the data from Paintal (1966) were used to interpolate rise and fall times of the models. The interpolated rise time values for RA, BF and SH are roughly 220 μs , 190 μs and 270 μs , respectively, whereas their fall times are longer and range from 350 μs to 365 μs . As a result, all three ANF models showed distinctly shorter rise times than interpolated values based on Paintal (1966). The fall time values of RA and BF were also smaller than results obtained by Paintal (1966), but the value of SH was about twice as much as the interpolated value.

3.4 Latency

The latency is defined as the time period between the onset of a stimulus and the peak of the resulting AP. Four monophasic cathodic stimuli differing in phase duration and stimulus amplitude were applied to the ANF models, and the corresponding latency was measured at the third dendritic node, which was right below the electrode. Results are listed in Tbl. 2 along with values from feline experiments. All models predicted a shorter latency than the experimental data for all considered stimuli, with RA in general having the closest values to experimental measurements, and BF producing significantly smaller latency values than the other models. This could partly be due to determining the latency at the compartment closest to the electrode in the model while, in the experiment, it might have been determined further away from the spike initiation site which would add an conduction delay. In both, experiment and model, increases in phase duration led to a longer latency, while an increase in the amplitude resulted in a shorter latency. Nevertheless, the data from Van den Honert and Stypulkowski (1984) suggests a latency reduction of around 50 % when doubling the stimulation current (Stim. B to Stim. C). RA and BF predicted a larger decrease of around 69 % and 66 % while SA predicted 57 %.

3.5 Refractoriness

The refractoriness characterizes the reduced excitability of an ANF after the initiation of an AP. It was measured in this study as described in Frijns et al. (1994): two monophasic 50 μs cathodic stimuli were applied. The first stimulus with an amplitude of $1.5I_{\text{th}}$ served as a masker for the second one; the current threshold of the second stimulus, necessary to elicit another AP, was measured for different inter-pulse intervals (IPI), i.e. the time period between the two stimuli (Wesselink et al., 1999).

Figure 8 depicts the refractoriness of the ANF models. In this figure, the relative increase in threshold of the second stimulus compared to a single pulse threshold is plotted against the IPI. At small IPI values,

the refractory curves of all models showed a steep decrease, where the thresholds of the second stimulus quickly approached the masker threshold. For IPI values around 2 ms, RA and SH predicted the threshold of the second pulse slightly smaller than the single pulse threshold.

The refractoriness of an ANF is usually described by the absolute and relative refractory periods (Wesselink et al., 1999): the absolute refractory period (ARP) is the time interval between two stimuli, during which the second stimulus required a current amplitude of at least 4 times the masker amplitude to elicit a second AP. On the other hand, the relative refractory period (RRP) is the time interval between the two stimuli, where the threshold of the second stimulus was only increased by a factor of 1.01. The ARP and RRP of ANF models for different stimuli are listed in Tbls. 3 & 4 along with values obtained in feline experiments. All models predicted a smaller RRP than the experimental measurements. Regarding ARP, a larger value than experimental observations was found in most conditions, except for a short ARP of 124 μ s acquired from BF for a biphasic stimulus of 50 μ s/phase. While the experimentally measured RRP values were approximately ten times larger than ARP, the ANF models predicted a ratio smaller than two.

3.6 Stochasticity

The stochasticity of ANFs can be described with two aspects: one is the jitter, defined as the standard deviation of repeated measurements of the latency; the other is the relative spread of the threshold I_{th} , calculated as the standard deviation of the threshold measurements divided by the mean (van Gendt et al., 2016). In this section, the Gaussian noise current term proposed by Rattay et al. (2001) was added to all three ANF models, as we wanted to investigate whether this simple and computationally efficient approach was sufficient to simulate the stochastic behavior within the range of experimental measurements. Monophasic 50 μ s cathodic current pulses were used for simulations, and stochastic behaviors were recorded for various values of k_{noise} , ranging from 0.1 to 2 times the initial value which was fitted in order to obtain a relative spread of about 5%. Threshold measurements for each k_{noise} value were repeated 500 times to calculate the relative spread. Jitters were obtained by measuring the latency 500 times for a stimulation with I_{th} . Spontaneous APs, i.e. APs initiated at 0 A or before the onset of the stimulus, were excluded in both measurements. Results are illustrated in Fig. 9.

For the selected range of k_{noise} the relative spread lied below 30 % for all models. Further increases in k_{noise} can result in larger spreads but also in a high probability for spontaneous APs. In comparison, results for the jitter were more varied. While the jitter could reach as far as to 180 μ s with RA, it was confined to 25 μ s in the case of the BF model.

Javel et al. (1987) reported a relative spread of 12 % and 11 % in feline ANFs using biphasic stimuli with phase durations of 200 μ s and 400 μ s, respectively. Smaller values between 5 % and 10 % were found by Miller et al. (1999) and Dynes (1996), who excited feline ANFs using monophasic pulses with a phase duration of 100 μ s and 40 μ s. Experimentally observed jitters for a stimulation of feline ANFs with I_{th} ranged from 80 μ s (Cartee et al., 2000) to 190 μ s (Van den Honert and Stypulkowski, 1984). Hence, the addition of Gaussian noise current to RA and SH with appropriate values for k_{noise} managed to produce both relative spread and jitter that fit the experimental range, as shown in Fig. 9. However, the jitter generated by BF was too small even for high k_{noise} values.

3.7 Pulse-train responses and adaptation

In this section, the spiking behavior of the ANF models was investigated for pulse-train stimulations. The Gaussian noise current term was again added to all models to account for the stochasticity. Biphasic current pulses with a phase duration of 20 μ s and an amplitude of 1.5 I_{th} were used.

306 The train of pulses lasted for 300 ms, and four different pulse rates were investigated. Each stimulation
307 was repeated 50 times. Poststimulus time histograms (PSTHs) were used to depict the average number of
308 APs in each 10 ms time bin in Fig. 10.

309 In general, higher pulse rates led to reduced firing efficiency. With a rate of 400 pps, 100 % firing
310 efficiency was obtained in all models. For an increase to 800 pps, RA and SH predicted reduced firing
311 rates. With a further increase to 2000 pps, RA showed a similar spiking behavior as for 800 pps, while
312 the spiking rate of BF was reduced by more than a factor of two, and SH responded almost solely to the
313 first pulses of the pulse trains. When stimulated with 5000 pps, small firing rates were measured with all
314 models.

315 Adaptation of ANF spiking rate has been demonstrated in animal experiments. Zhang et al. (2007)
316 measured adaptive responses to pulse trains with rates between 250 and 10 000 pps, and reported that the
317 reduction in firing rates became larger as pulse rates increased. A similar tendency was observed by Litvak
318 et al. (2001), who applied pulse-train stimuli with rates of 1200 and 4800 pps. Zhang et al. (2007) and
319 Westerman and Smith (1984) concluded using feline and gerbil ANFs that adaptation was strongest during
320 the first 10 ms of a pulse train, but still apparent after 100 ms. As none of the ANF models used in this study
321 was explicitly developed to include adaptation, it is unsurprising that they showed no or little adaptation
322 mostly limited to a reduction in firing efficiency following the first AP.

4 SUMMERY AND CONCLUSION

323 In this study, we designed a computational framework to investigate some properties of biophysical multi-
324 compartment models of the human ANF. We subsequently implemented three existing cable models in this
325 framework, including RA Rattay et al. (2001), BF Briaire and Frijns (2005) and SH Smit et al. (2010), and
326 compared the outcomes with each other and with experimental measurements. This is the first study to
327 perform a systematic comparison between different multi-compartment models of the human ANF, and
328 will contribute to the future development of ANF models.

329 In comparison to experimental data, ANF models predicted drastically smaller ratios between ARP and
330 RRP values as they revealed an overestimated ARP and an underestimated RRP. With axon models by
331 Frijns et al. (1994) and Imennov and Rubinstein (2009), distinctly higher ratios of RRP to ARP have
332 been predicted (detailed results not shown). A likely explanation for the more physiologically accurate
333 refractoriness of axon models is the simplified morphology, particularly the lack of a soma. Moving the
334 stimulus location for the human ANF models from dendrite to axon and therefore excluding the impact of
335 the soma would have resulted in less steep refractory curves and higher ratios of RRP to ARP.

336 One major hindrance regarding human ANF modelling is that neither the precise morphology nor the ion
337 channel kinetics of human neurons are completely characterized (O'Brien and Rubinstein, 2016). Neverth-
338 eless, the inclusion of a soma is crucial for a realistic description of the human ANF. The unmyelinated
339 soma in human ANF models is highly capacitive and thus charge consuming which imposes a huge barrier
340 for the propagation of an AP. This leads to a large delay in propagation. Rattay et al. (2001) mentioned that
341 the somatic barrier became insurmountable for APs after only small variations of certain model parameters.
342 This reveals the difficulty of balancing the capacity of the soma in order to predict a realistic somatic delay
343 without erasing the AP. Even small changes in the stimulation pattern such as an increase of the IPI for
344 a few microseconds can cause the loss of the second AP at the somatic region, which explains the very
345 steep refractory curves as shown in Fig. 8. Somas in feline ANF models are less critical for the propagation
346 of APs as they are small and myelinated (Liberman and Oliver, 1984), which reduces the capacity and in

turns the chance of losing an AP at the somatic region. In addition, the inclusion of a soma necessitates the addition of a dendrite; this further complicates the optimization of an already large set of parameters in biophysical ANF models.

In this study, the Gaussian noise current term in RA was also applied to the other two models to account for the stochastic nature of ion channels. Based on Eq. 1, this noise current increases with the maximum sodium conductivity and the membrane surface area, implying that stochasticity is more pronounced in larger fibers and with higher sodium densities. However, the contrary has been revealed in experiments: the strength of stochasticity was found to decrease as the fiber diameter increased (Verveen, 1962), and the relative spread was later demonstrated to be inversely proportional to the square root of the total number of sodium channels (Rubinstein, 1995). As a consequence, the role of a single channel in the voltage fluctuation is less significant when compared to the total ionic conductance (Rubinstein, 1995; Badenhorst et al., 2016). Moreover, experiments showed that the ionic channel noise of ANF increased as the membrane potential deviated from the resting potential (Verveen and Derksen, 1968), but such voltage dependency was not included in the noise current term by Rattay et al. (2001). A modified version of the conductance-based stochastic model, which included the inverse relationship and voltage dependency, has been proposed by Badenhorst et al. (2016). Here, the authors were particularly motivated to have their model reflect the actual *in vivo* behaviors. The single node model by Negm and Bruce (2014) and the axon model by Imennov and Rubinstein (2009) produced stochastic responses using a channel number tracking algorithm with channel transitions following a Markov jumping process. This approach was found to be the most accurate one to model channel noise Mino et al. (2002). It is hence worth to further investigate the applicability of these approaches in our framework.

None of the three models predicted pulse-train responses in a range comparable with experimental results, because they were not able to appropriately account for temporal effects of ANF, such as pulse-train integration or adaptation. Therefore, these models need to incorporate a mechanism capable of predicting such long-term effects, as these effects are likely to exert a significant impact on the perception of CI users (Clay and Brown, 2007).

Currently, there is still no precise knowledge regarding the mechanisms of the adaptive behavior observed in ANFs. Nevertheless, two biophysical approaches for adaptation have been developed. Woo et al. (2009) modeled adaptation using a dynamic external potassium concentration $[K^+]_e$ at the nodes of Ranvier, and applied it to a feline ANF model in Woo et al. (2010). The model was based on the findings on leeches that $[K^+]_e$ changes induced adaptation-like effects (Baylor and Nicholls, 1969). However, there is no experimental evidence that an ongoing stimulation of a nerve fiber can alter $[K^+]_e$ sufficiently, or that this is the case in mammal ANFs.

Negm and Bruce (2014) incorporated adaptation in a single node model by adding hyperpolarization-activated cation channels and low-threshold potassium channels, both of which have been identified in mammalian spiral ganglion neurons. These two types of ion channels had a much slower gating property and complemented the relatively fast dynamics of sodium and potassium currents. As this approach has not yet been applied to a multi-compartment ANF model, it remains unclear how the additional ion channels will affect the initiation and propagation of APs. A simple inclusion of these channels to an existing ANF model is not sufficient, as the spiking behavior of the model may be altered, and subsequently extensive parameter optimization is required.

On the other hand, stochasticity and temporal behaviors of ANF have been efficiently implemented in phenomenological models. van Gendt et al. (2016) created a hybrid model that combined the biophysical

and phenomenological approaches to efficiently predict responses to pulse-train stimuli. This model was also implemented in combination with a three-dimensional volume conduction model of the cochlea (van Gendt et al., 2016, 2017). Nonetheless, as phenomenological models do not include realistic biophysical details in their implementation, their predictions are often limited only to predefined stimuli.

5 CONFLICT OF INTEREST STATEMENT

The authors declare that the research was conducted in the absence of any commercial or financial relationships that could be construed as a potential conflict of interest.

6 AUTHOR CONTRIBUTIONS

RB contributed to model simulation, data acquisition and analysis, and manuscript drafting. JE contributed to study design, data analysis and manuscript revising. MO contributed to data analysis and manuscript revising. WH and SB contributed to study design and critical manuscript revising. The final manuscript has been approved by all authors.

7 FUNDING

This project received funding from the European Union's Horizon 2020 research and innovation program under the Marie Skłodowska-Curie grant agreement No 702030 and from the DFG (HE67132-1). JE was supported by a DFG grant within the PP1608 Ultrafast and temporally precise information processing: normal and dysfunctional hearing (HE6713/1-1 and 1-2).

DATA AVAILABILITY STATEMENT

The scripts and generated datasets for this study can be found at <https://gitlab.lrz.de/tueibai-public/human-anf-models.git>.

REFERENCES

- Armstrong, D., Harvey, R., and Schild, R. F. (1973). The Spatial Organisation of Climbing Fibre Branching in the Cat Cerebellum. *Experimental Brain Research* 58, 40–58
- Badenhorst, W., Hanekom, T., and Hanekom, J. J. (2016). Development of a voltage-dependent current noise algorithm for conductance-based stochastic modelling of auditory nerve fibres. *Biological Cybernetics* 110, 403–416. doi:10.1007/s00422-016-0694-6
- Baylor, D. A. and Nicholls, J. (1969). Changes in extracellular potassium concentration produced by neuronal activity in the central nervous system of the leech. *Journal of Physiology* , 555–569
- BeMent, S. L. and Ranck, J. B. (1969). Quantitative Study Central of Electrical Stimulation Fibers of Myelinated. *Experimental Neurology* 170, 147–170
- Blight, A. R. (1985). Computer simulation and afterpotentials in axons: the case for a lower resistance myelin sheath. *Neuroscience* 15, 13–31
- Boyd, I. and Kalu, K. (1979). Scaling factor relating conduction velocity and diameter for myelinated afferent nerve fibres in the cat hind limb. *Journal of Physiology* , 277–297
- Briaire, J. J. and Frijns, J. H. (2005). Unraveling the electrically evoked compound action potential. *Hearing Research* 205, 143–156. doi:10.1016/j.heares.2005.03.020

- 421 Brown, C. J. and Abbas, P. J. (1990). Electrically evoked whole-nerve action potentials : Parametric data
422 from the cat. *Acoustical Society of America* 2205. doi:10.1121/1.400117
- 423 Carlyon, R. P., Deeks, J. M., and McKay, C. M. (2015). Effect of Pulse Rate and Polarity on the Sensitivity
424 of Auditory Brainstem and Cochlear Implant Users to Electrical Stimulation. *JARO - Journal of the*
425 *Association for Research in Otolaryngology* 668, 653–668. doi:10.1007/s10162-015-0530-z
- 426 Cartee, L. A., Van Den Honert, C., Finley, C. C., and Miller, R. L. (2000). Evaluation of a model of
427 the cochlear neural membrane. I. Physiological measurement of membrane characteristics in response
428 to intrameatal electrical stimulation. *Hearing Research* 146, 143–152. doi:10.1016/S0378-5955(00)
429 00109-X
- 430 Clay, K. M. and Brown, C. J. (2007). Adaptation of the Electrically Evoked Compound Action Potential
431 (ECAP) Recorded from Nucleus CI24 Cochlear Implant Users. *Ear & Hearing*
- 432 Dynes, S. B. C. and Delgutte, B. (1992). Phase-locking of auditory-nerve discharges to sinusoidal electric
433 stimulation of the cochlea. *Hearing Research* 58, 79–90
- 434 Dynes, S. B. S. (1996). *Discharge Characteristics of Auditory Nerve Fibers for Pulsatile Electrical*
435 *Stimuli.pdf*. Ph.D. thesis, Massachusetts institute of technology
- 436 Frankenhaeuser, B. and Huxley, A. F. (1964). The action potential in the myelinated nerve fibre of *Xenopus*
437 *laevis* as computed on the basis of voltage clamp data. *J.Physiol* , 302–315
- 438 Frijns, J. H. M., Desnoo, S. L., and Schonhooven, R. (1995). Potential distribution and neural excitation
439 patterns in rotationally symmetrical model of the electrically stimulated cochlea. *Hearing Research* 87,
440 170–186
- 441 Frijns, J. H. M., Mooij, J., and Kate, J. H. (1994). A Quantitative Approach to Modeling Mammalian
442 Myelinated Nerve Fibers for Electrical Prosthesis Design. *IEEE Transactions on Biomedical Engineering*
443 41, 556–566
- 444 Goodman, D. F. M. and Brette, R. (2009). The Brian simulator. *frontiers in Neuroscience* 3, 192–197.
445 doi:10.3389/neuro.01.026.2009
- 446 Hartmann, R., Topp, G., and Klinke, R. (1984). Discharge patterns of cat primary auditory nerve fibers
447 with electrical stimulation of the cochlea. *Hearing Research* 13, 47–62
- 448 Hodgkin, A. L. and Huxley, A. F. (1952). A quantitative description of membrane current and its application
449 to conduction and excitation in nerve. *J.Physiol* , 500–544
- 450 Hursh, J. (1939). Conduction velocity and diameter of nerve fibers. *American Physiological Society*
- 451 Imennov, N. S. and Rubinstein, J. T. (2009). Stochastic population model for electrical stimulation of the
452 auditory nerve. *IEEE Transactions on Biomedical Engineering* 56, 2493–2501. doi:10.1109/TBME.
453 2009.2016667
- 454 Javel, E., Tong, Y., Shepherd, R. K., and Clark, G. M. (1987). Responses of cat auditory nerve fibers to
455 biphasic electrical current pulses. *Physiology and Psychophysics*
- 456 Kalkman, R. K., Briaire, J. J., Dekker, D. M. T., and Frijns, J. H. M. (2014). Place pitch versus electrode
457 location in a realistic computational model of the implanted human cochlea. *Hearing Research* 315,
458 10–24. doi:10.1016/j.heares.2014.06.003
- 459 Kalkman, R. K., Briaire, J. J., and Frijns, J. H. M. (2015). Current focussing in cochlear implants: An
460 analysis of neural recruitment in a computational model. *Hearing Research* 322, 89–98. doi:10.1016/j.
461 heares.2014.12.004
- 462 Lai, W. K. and Dillier, N. (2000). A Simple Two-Component Model of the Electrically Evoked Compound
463 Action Potential in the Human Cochlea. *Zurich Open Repository and Archive* 5, 333–345
- 464 Liberman, M. and Oliver, M. (1984). Morphometry of intracellularly labeled neurons of the auditory nerve:
465 correlations with functional properties. *Journal of Computational Neuroscience*

- 466 Litvak, L., Delgutte, B., and Eddington, D. (2001). Auditory nerve fiber responses to electric stimulation :
 467 Modulated and unmodulated pulse trains. *Acoustical Society of America* 368. doi:10.1121/1.1375140
- 468 Malherbe, T. K., Hanekom, T., and Hanekom, J. J. (2016). Constructing a three-dimensional electrical
 469 model of a living cochlear implant user ' s cochlea. *International Journal for Numerical Methods in*
 470 *Biomedical Engineering* , 1–23doi:10.1002/cnm
- 471 Miller, C. A., Abbas, P. J., and Robinson, B. K. (2001). Response Properties of the Refractory Auditory
 472 Nerve Fiber. *Journal of the Association for Research in Otolaryngology* 2, 216–232. doi:10.1007/
 473 s101620010083
- 474 Miller, C. A., Abbas, P. J., and Rubinstein, J. T. (1999). An empirically based model of the electrically
 475 evoked compound action potential. *Hearing Research* 135, 1–18. doi:10.1016/S0378-5955(99)00081-7
- 476 Mino, H., Rubinstein, J. T., and White, J. A. (2002). Comparison of algorithms for the simulation of
 477 action potentials with stochastic sodium channels. *Annals of Biomedical Engineering* 30, 578–587.
 478 doi:10.1114/1.1475343
- 479 Negm, M. H. and Bruce, I. C. (2014). The effects of HCN and KLT ion channels on adaptation and
 480 refractoriness in a stochastic auditory nerve model. *IEEE Transactions on Biomedical Engineering* 61,
 481 2749–2759. doi:10.1109/TBME.2014.2327055
- 482 Nogueira, W. and Ashida, G. (2018). Development of a Parametric Model of the Electrically Stimulated
 483 Auditory Nerve. *Springer* 84. doi:10.1007/978-3-319-59548-1
- 484 O'Brien, G. E. and Rubinstein, J. T. (2016). The development of biophysical models of the electrically
 485 stimulated auditory nerve: Single-node and cable models. *Network: Computation in Neural Systems* 27,
 486 135–156. doi:10.3109/0954898X.2016.1162338
- 487 Paintal, A. S. (1966). The influence of diameter of medullated nerve fibres of cats on the rising and falling
 488 phases of the spike and its recovery. *Journal of Physiology* , 791–811
- 489 Pfingst, B. E. (1988). Comparisons of psychophysical and neurophysiological studies of cochlear implants.
 490 *Hearing Research* 34, 243–251
- 491 Pfingst, B. E. and Morris, D. J. (1993). Stimulus features affecting psychophysical detection thresholds
 492 for electrical stimulation of the cochlea . II : Frequency and interpulse interval. *The Journal of the*
 493 *Acoustical Society of America* 1287. doi:10.1121/1.408155
- 494 Ranck, J. B. J. (1975). Which elements are excited in electrical stimulation of mammalian central nervous
 495 system. *Brain Research* 98
- 496 Rattay, F., Leao, R. N., and Felix, H. (2001). A model of the electrically excited human cochlear neuron I.
 497 Contribution of neural substructures to the generation and propagation of spikes. *Hearing Research* 153,
 498 64–79. doi:10.1016/S0378-5955(00)00257-4
- 499 Rubinstein, J. T. (1995). Threshold fluctuations in an N sodium channel model of the node of Ranvier.
 500 *Biophysical Journal* 68, 779–785. doi:10.1016/S0006-3495(95)80252-3
- 501 Schwarz, J. R. and Eikhof, G. (1987). Na currents and action potentials in rat myelinated nerve fibres at 20
 502 and 37 C. *European Journal of Physiology* , 569–577
- 503 Schwarz, J. R., Reid, G., and Bostock, H. (1995). Action potentials and membrane currents in the
 504 human node of Ranvier. *Pflugers Archiv European Journal of Physiology* 430, 283–292. doi:10.1007/
 505 BF00374660
- 506 Shannon, R. V. (1983). Multichannel electrical stimulation of the auditory nerve in man . I . Basic
 507 psychophysics. *Hearing Research* 11, 157–189
- 508 Smit, J. E., Hanekom, T., and Hanekom, J. J. (2008). Predicting action potential characteristics of human
 509 auditory nerve fibres through modification of the Hodgkin – Huxley equations. *South African Journal of*
 510 *Science* , 3–8

- 511 Smit, J. E., Hanekom, T., and Hanekom, J. J. (2009). Modelled temperature-dependent excitability
512 behaviour of a generalised human peripheral sensory nerve fibre. *Biological Cybernetics* 101, 115–130.
513 doi:10.1007/s00422-009-0324-7
- 514 Smit, J. E., Hanekom, T., van Wieringen, A., Wouters, J., and Hanekom, J. J. (2010). Threshold predictions
515 of different pulse shapes using a human auditory nerve fibre model containing persistent sodium and
516 slow potassium currents. *Hearing Research* 269, 12–22. doi:10.1016/j.heares.2010.08.004
- 517 Stypulkowski, P. H. and Van den Honert, C. (1984). Physiological properties of the electrically stimulated
518 auditory nerve. I. Compound action potential recordings. *Hear Res* 14, 205–223
- 519 Van den Honert, C. and Stypulkowski, P. H. (1984). Physiological properties of the electrically stimulated
520 auditory nerve. II. Single fiber recordings. *Hear Research* 14, 205–223
- 521 van Gendst, M. J., Briaire, J. J., Kalkman, R. K., and Frijns, J. H. (2016). A fast, stochastic, and adaptive
522 model of auditory nerve responses to cochlear implant stimulation. *Hearing Research* 341, 130–143.
523 doi:10.1016/j.heares.2016.08.011
- 524 van Gendst, M. J., Briaire, J. J., Kalkman, R. K., and Frijns, J. H. M. (2017). Modeled auditory nerve
525 responses to amplitude modulated cochlear implant stimulation. *Hearing Research* 351, 19–33. doi:10.
526 1016/j.heares.2017.05.007
- 527 Verveen, A. A. (1962). Axon diameter and fluctuation in excitability. *ACTA MORPHOLOGICA*
528 *NEERLANDO-SCANDINAVICA* V
- 529 Verveen, A. A. and Derksen, H. E. (1968). Fluctuation Phenomena in Nerve Membrane. *Proceedings of*
530 *the IEEE* 56, 906–916. doi:10.1109/PROC.1968.6443
- 531 Wesselink, W. A., Holsheimer, J., and Boom, H. B. (1999). A model of the electrical behaviour of
532 myelinated sensory nerve fibres based on human data. *Med.Biol.Eng Comput.* 37, 228–235. doi:10.
533 1007/BF02513291
- 534 Westerman, L. A. and Smith, R. L. (1984). Rapid and short-term adaptation in auditory nerve responses.
535 *Hearing Research* 15, 249–260
- 536 Woo, J., Miller, C., and Abbas, P. (2009). Biophysical Model of an Auditory Nerve Fiber With a Novel
537 Adaptation Component. *IEEE Transactions on Biomedical Engineering* 56, 2177–2180. doi:10.1109/
538 TBME.2009.2023978
- 539 Woo, J., Miller, C. A., and Abbas, P. J. (2010). The dependence of auditory nerve rate adaptation on electric
540 stimulus parameters, electrode position, and fiber diameter: A computer model study. *JARO - Journal of*
541 *the Association for Research in Otolaryngology* 11, 283–296. doi:10.1007/s10162-009-0199-2
- 542 Zhang, F., Miller, C. A., Robinson, B. K., Abbas, P. J., and Hu, N. (2007). Changes across time in spike
543 rate and spike amplitude of auditory nerve fibers stimulated by electric pulse trains. *JARO - Journal of*
544 *the Association for Research in Otolaryngology* 8, 356–372. doi:10.1007/s10162-007-0086-7
- 545 Zhou, N., Kraft, C. T., Colesa, D. J., and Pfingst, B. E. (2015). Integration of Pulse Trains in Humans and
546 Guinea Pigs with Cochlear Implants. *Journal of the Association for Research in Otolaryngology* 534,
547 523–534. doi:10.1007/s10162-015-0521-0

Table 1. Rheobase I_{rh} and chronaxie τ_{chr} of ANF models for monophasic cathodic and anodic stimulation.

	$I_{rh}/\mu A$		$\tau_{chr}/\mu s$	
	cathodic	anodic	cathodic	anodic
Rattay model	61.3	83.4	125	122
Briaire-Frijns model	220	464	39.1	39.1
Smit-Hanekom model	64.7	79	93.8	85.9

Table 2. Action potential latency of ANF models measured with four different stimuli. Latency values from relevant feline studies are also included (italicized).

	Stim. A	Stim. B	Stim. C	Stim. D
Rattay model	275 μs	283 μs	87 μs	323 μs
Briaire-Frijns model	140 μs	148 μs	50 μs	193 μs
Smit-Hanekom model	261 μs	267 μs	115 μs	298 μs
<i>Cartee et al. (2000)</i>	440 μs	-	-	-
<i>Van den Honert and Stypulkowski (1984)</i>	-	685 μs	352 μs	-
<i>Miller et al. (1999)</i>	-	-	-	650 μs

Table 2. A: monophasic 40 μs cathodic current pulse with amplitude I_{th}

B: monophasic 50 μs cathodic current pulse with amplitude I_{th}

C: monophasic 50 μs cathodic current pulse with amplitude $2I_{th}$

D: monophasic 100 μs cathodic current pulse with amplitude I_{th}

Table 3. Absolute refractory period of ANF models measured with four stimuli. Measurements from feline studies are also included (italicized).

	Stim. A	Stim. B	Stim. C	Stim. D
Rattay model	1381 μs	1372 μs	1333 μs	1331 μs
Briaire-Frijns model	1261 μs	1262 μs	1224 μs	124 μs
Smit-Hanekom model	2151 μs	2143 μs	2105 μs	2139 μs
<i>Miller et al. (2001)</i>	334 μs	-	-	-
<i>Stypulkowski and Van den Honert (1984)</i>	-	300 μs	-	-
<i>Dynes (1996)</i>	-	-	500 μs to 700 μs	-
<i>Brown and Abbas (1990)</i>	-	-	-	500 μs

Table 3. A: monophasic 40 μs cathodic current pulses

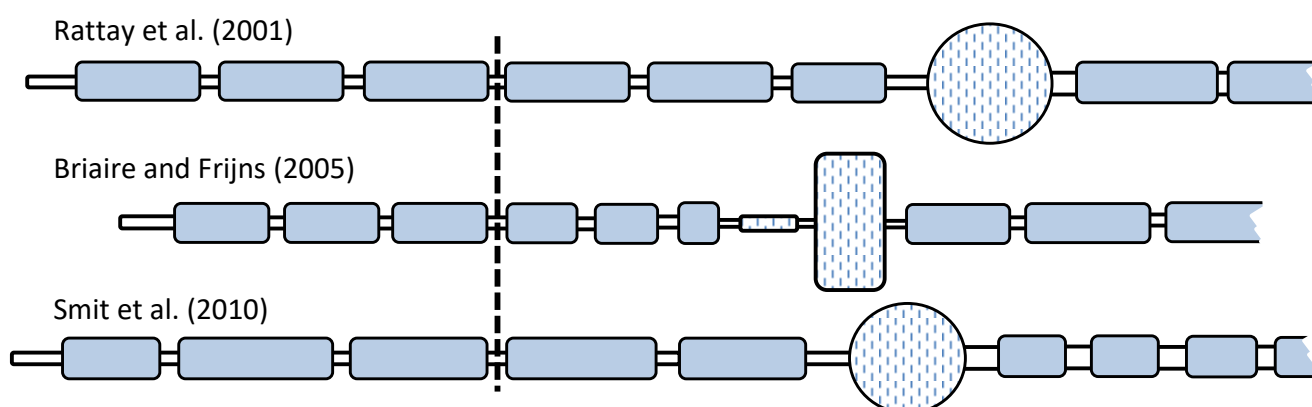
B: monophasic 50 μs cathodic current pulses

C: monophasic 100 μs cathodic current pulses

D: biphasic 50 μs cathodic first current pulses

Table 4. Relative refractory period of ANF models measured with four stimuli. Measurements from feline studies are also included (italicized).

	Stim. A	Stim. B	Stim. C
Rattay model	1.82 ms	1.77 ms	1.28 ms
Briaire-Frijns model	2.43 ms	2.55 ms	2.45 ms
Smit-Hanekom model	2.14 ms	2.11 ms	1.89 ms
<i>Stypulkowski and Van den Honert (1984)</i>	3 ms to 4 ms	-	-
<i>Cartee et al. (2000)</i>	4 ms to 5 ms	-	-
<i>Dynes (1996)</i>	-	5 ms	-
<i>Hartmann et al. (1984)</i>	-	-	5 ms

Table 4. A: monophasic 50 μ s cathodic current pulsesB: monophasic 100 μ s cathodic current pulsesC: biphasic 200 μ s cathodic first current pulses**Figure 1.** Comparison of the ANF morphologies. All dendrites and axons were myelinated, denoted by the blue color. The somas of all three models were unmyelinated but surrounded by layers of “satellite cells”, as described in Rattay et al. (2001), and so was the pre-somatic region of the BF model. Relative differences in compartment size among the three models are indicated in the figure, but they are not true to scale. Vertical line indicates the position of the stimulation electrode (distance from the neuron was 500 μ m).

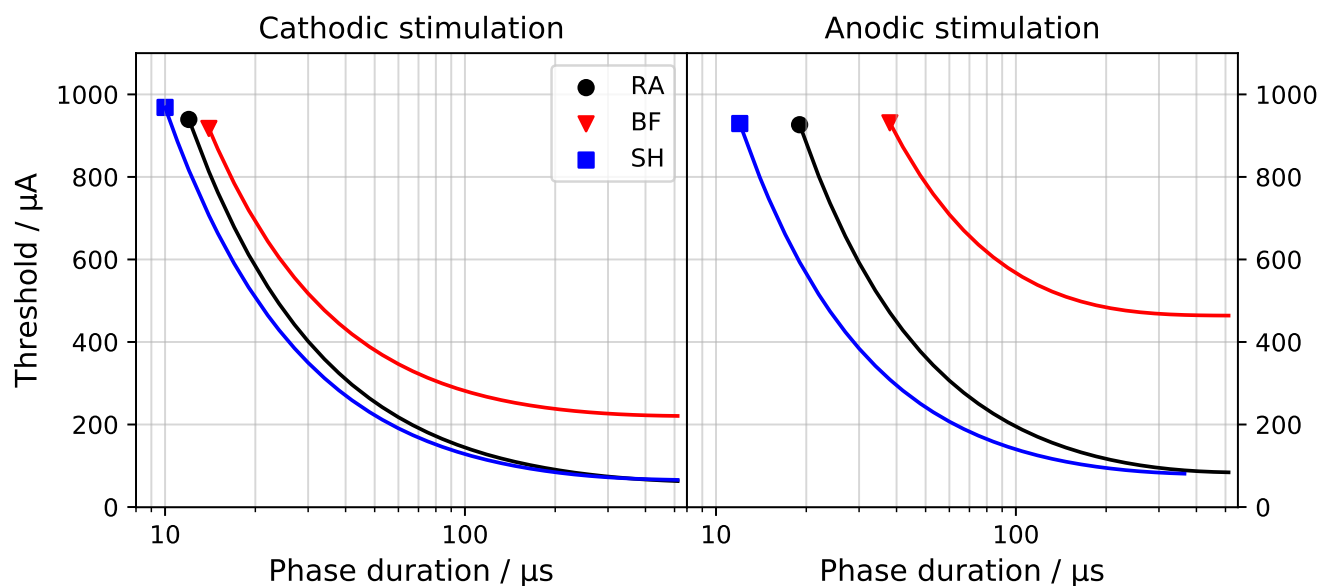


Figure 2. Strength-duration curves for monophasic cathodic (left) and anodic (right) stimuli. “RA”, “BF” and “SH” denote the Rattay, Briaire-Frijns and Smit-Hanekom models, respectively. The x -axis is set in a log-scale for a better comparison.

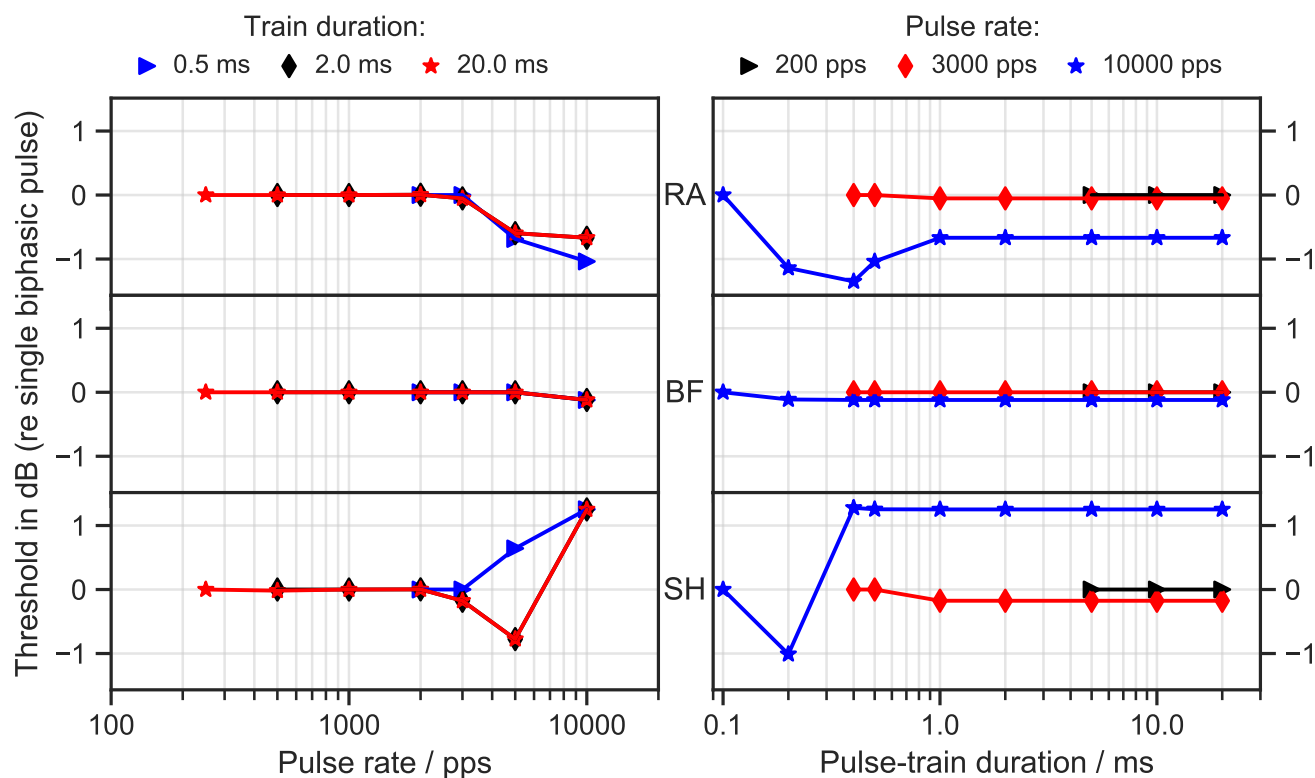


Figure 3. Threshold as a function of pulse rate (left column) and pulse-train duration (right column). RA: Rattay model; BF: Briaire-Frijns model; SH: Smit-Hanekom model. The stimulation current was a train of biphasic cathodic-first $45 \mu\text{s}$ pulses with an inter-phase gap of $8 \mu\text{s}$. The threshold is reported in dB as the ratio of I_{th} for the pulse train to I_{th} for a single biphasic pulse.

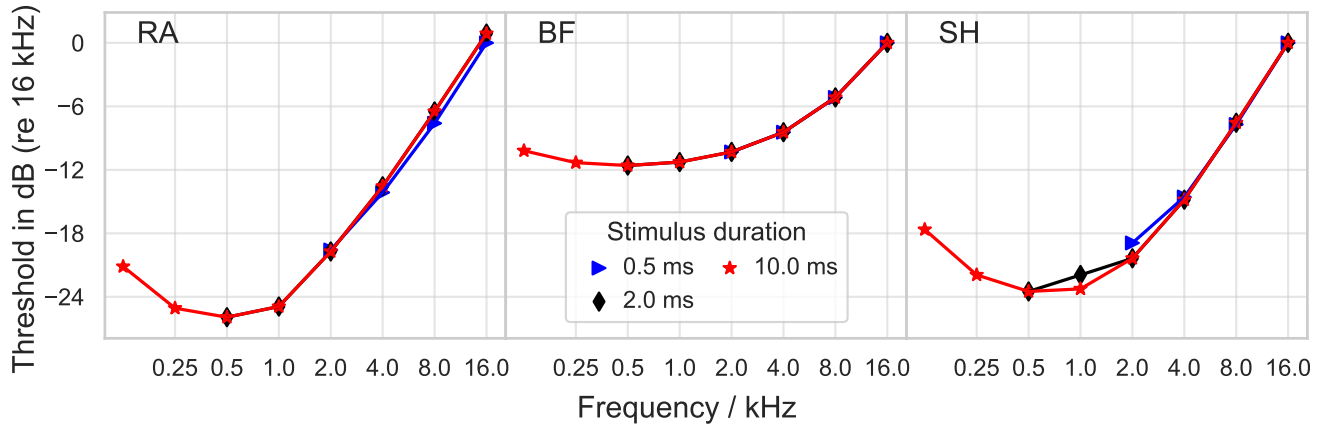


Figure 4. Threshold for sinusoidal stimulation as a function of stimulus frequency. The threshold is reported in dB as the ratio to I_{th} at the frequency of 16 kHz. “RA”, “BF” and “SH” denote the Rattay, Briaire-Frijns and Smit-Hanekom models, respectively. All results are plotted for three stimulus durations.

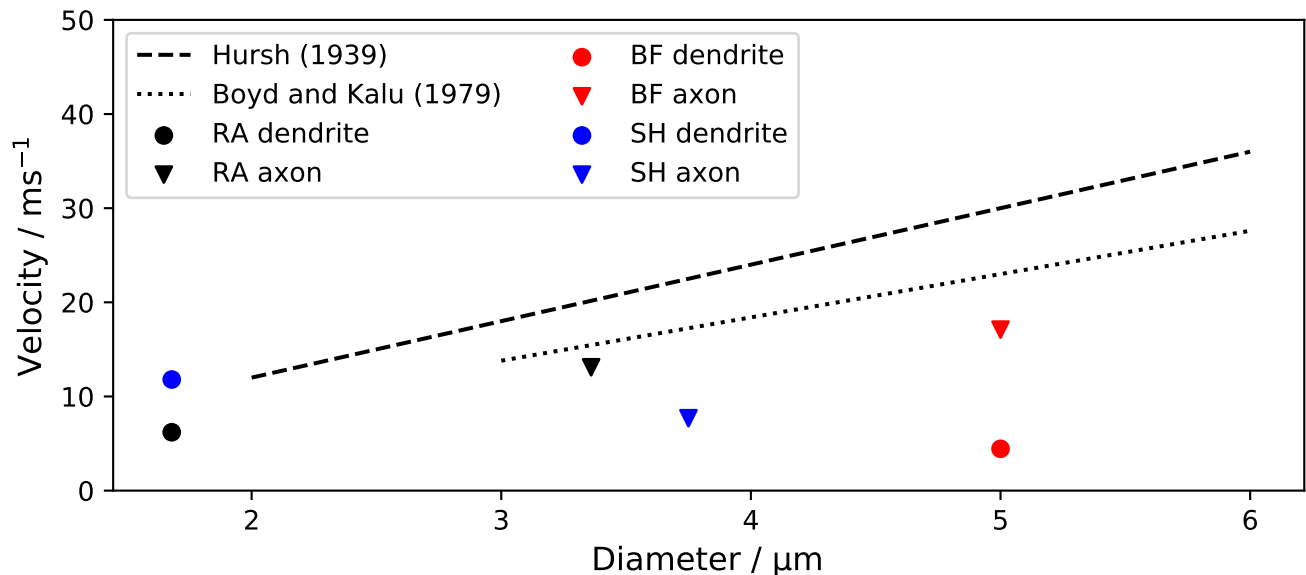


Figure 5. Conduction velocity v_c of ANF models in comparison to experimental data. The velocities of dendrite and axon of each model were measured separately due to their morphological and physiological differences. v_c is plotted against the fiber outer diameters. “RA”, “BF” and “SH” denote the Rattay, Briaire-Frijns and Smit-Hanekom models, respectively.

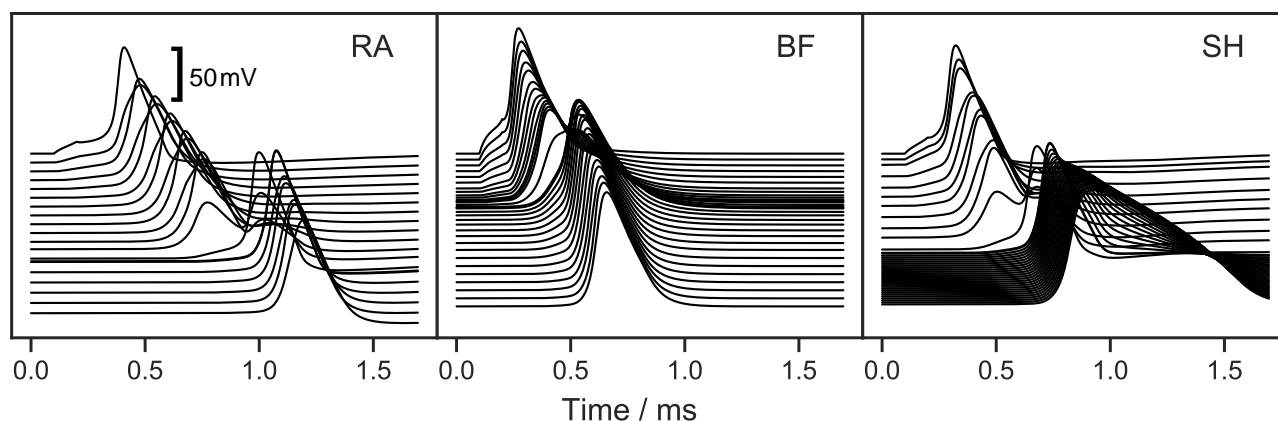


Figure 6. Response of ANF models to a 100 μ s cathodic current pulse injected at the peripheral terminal. “RA”, “BF” and “SH” denote the Rattay, Briare-Frijns and Smit-Hanekom models, respectively. Each line depicts the voltage over a course of time at a single morphologic component, starting from the peripheral terminal represented by the topmost line. The lines are vertically aligned true to scale according to the compartmental distances. The high capacitance of the causes a large additional delay of the AP.

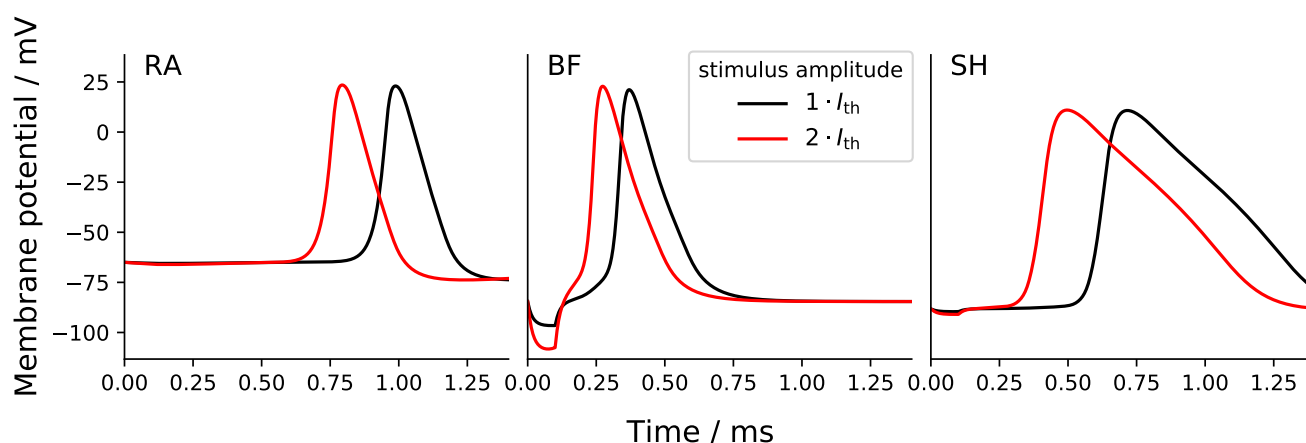


Figure 7. Transmembrane voltage (action potential) at the tenth axonal node of the ANF models to a monophasic 100 μ s cathodic current pulse with an amplitude of I_{th} and $2 \times I_{th}$. “RA”, “BF” and “SH” denote the Rattay, Briare-Frijns and Smit-Hanekom models, respectively.

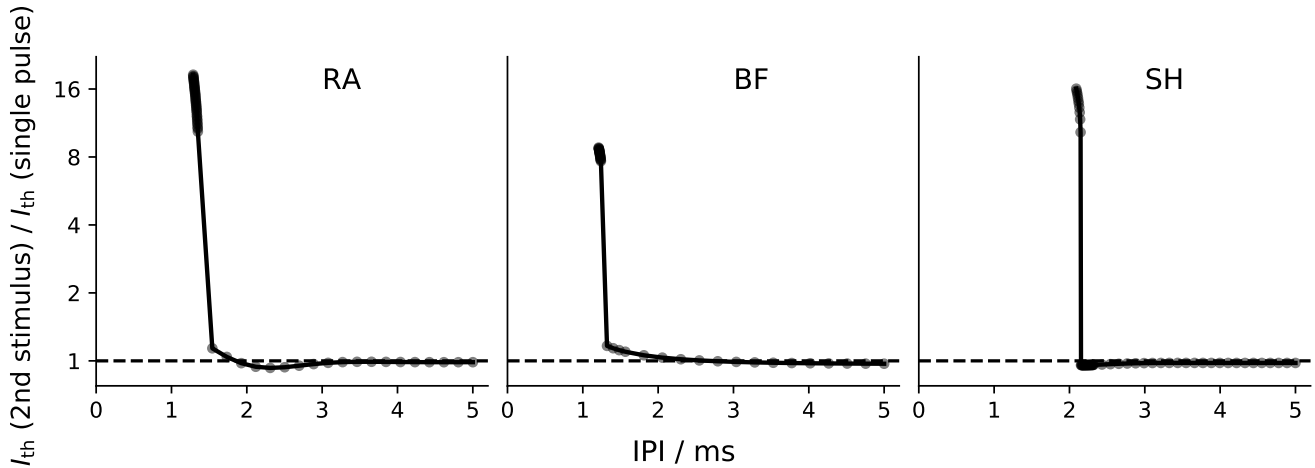


Figure 8. Refractory curve of ANF models. Both the masker and the second stimulus were a monophasic cathodic pulse with a phase length of $50\ \mu\text{s}$. “RA”, “BF” and “SH” denote the Rattay, Briaire-Frijns and Smit-Hanekom models, respectively. Please notice that the scaling of the y -axis is logarithmic.

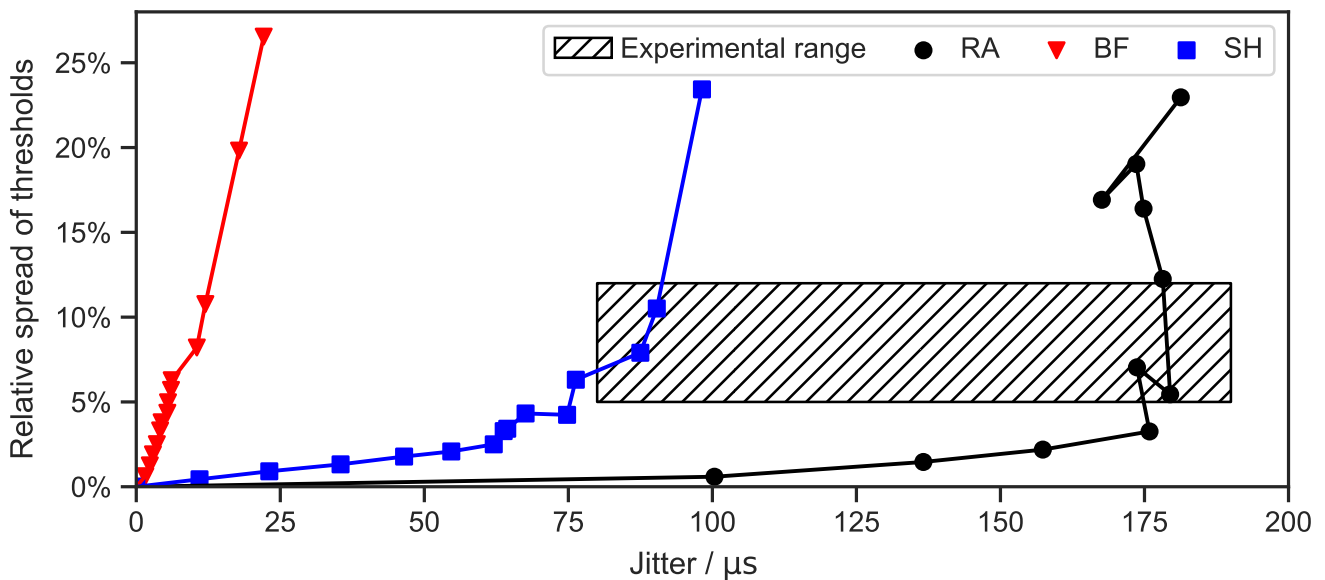


Figure 9. Stochasticity of ANF models with a Gaussian noise current term. Jitter and relative spread of threshold were measured for different values of k_{noise} . A monophasic $50\ \mu\text{s}$ cathodic current pulse was applied in each simulation. Threshold and latency were measured 100 and 500 times, respectively, for each datapoint. “RA”, “BF” and “SH” denote the Rattay, Briaire-Frijns and Smit-Hanekom models, respectively. The experimental range was summarised from a series of animal experiments, including Van den Honert and Stypulkowski (1984), Javel et al. (1987), Dynes (1996), Miller et al. (1999) and Cartee et al. (2000).

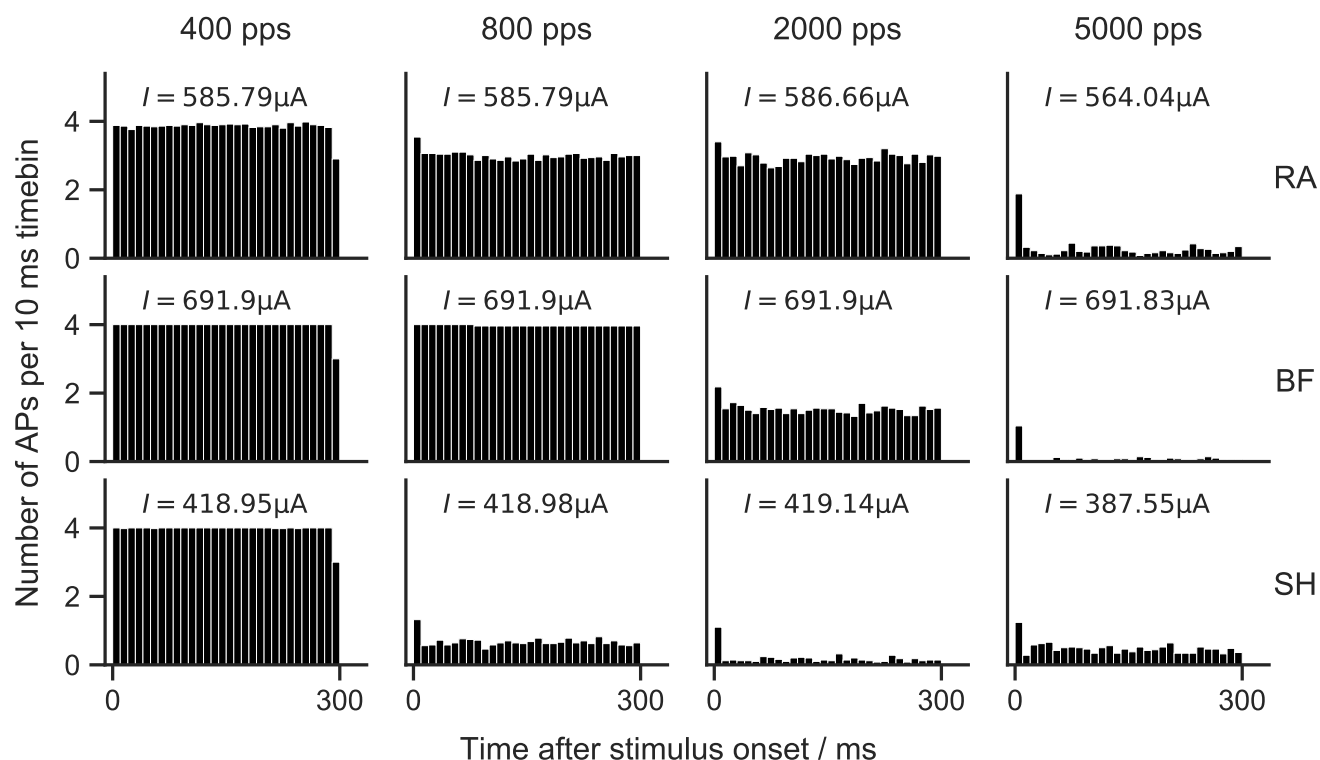


Figure 10. Poststimulus time histograms of ANF models to 300 ms pulse-train stimulation. **RA**: Rattay model; **BF**: Briaire-Frijns model; **SH**: Smit-Hanekom model. Biphasic (cathodic-first) current pulses with a phase duration of $20\mu\text{s}$ and an amplitude of I_{th} were used for pulse-trains with four different pulse rates. Each stimulation was repeated 50 times. Vertical columns in PSTHs show the average number of APs in a 10 ms time bin.